

**REPORT DOCUMENTATION PAGE**Form Approved  
OMB No. 0704-0188

Public reporting burden for this collection of information is estimated to average 1 hour per response, including the time for reviewing instructions, searching existing data sources, gathering and maintaining the data needed, and completing and reviewing this collection of information. Send comments regarding this burden estimate or any other aspect of this collection of information, including suggestions for reducing this burden to Department of Defense, Washington Headquarters Services, Directorate for Information Operations and Reports (0704-0188), 1215 Jefferson Davis Highway, Suite 1204, Arlington, VA 22202-4302. Respondents should be aware that notwithstanding any other provision of law, no person shall be subject to any penalty for failing to comply with a collection of information if it does not display a currently valid OMB control number. PLEASE DO NOT RETURN YOUR FORM TO THE ABOVE ADDRESS.

**1. REPORT DATE (DD-MM-YYYY)**

13-05-2004

REPRINT

**4. TITLE AND SUBTITLE**

On the Linear Theory of Equatorial Plasma Instability:  
Comparison of Different Descriptions

**5a. CONTRACT NUMBER****5b. GRANT NUMBER****5c. PROGRAM ELEMENT NUMBER**

61102F

**6. AUTHOR(S)**

B. Basu

**5d. PROJECT NUMBER**

2311

**5e. TASK NUMBER**

SD

**5f. WORK UNIT NUMBER**

A3

**7. PERFORMING ORGANIZATION NAME(S) AND ADDRESS(ES)**

Air Force Research Laboratory/VSBXP  
29 Randolph Road  
Hanscom AFB MA 01731-3010

**8. PERFORMING ORGANIZATION REPORT**

20040526 048

**9. SPONSORING / MONITORING AGENCY NAME(S) AND ADDRESS(ES)****10. SPONSOR/MONITOR'S ACRONYM(S)**  
AFRL/VSBXP**11. SPONSOR/MONITOR'S REPORT  
NUMBER(S)**

AFRL-VS-HA-TR-2004-1075

**12. DISTRIBUTION / AVAILABILITY STATEMENT**

Approved for Public Release; Distribution Unlimited.

**13. SUPPLEMENTARY NOTES**

REPRINTED FROM: JOURNAL OF GEOPHYSICAL RESEARCH, Vol 107, No. A8, 10.1029/2001JA000317, 2002.

**14. ABSTRACT**

[1] Three theoretical descriptions, namely, the local description, the flux tube integrated description and the ballooning-mode type description, of the equatorial plasma instability are presented for comparisons. On the basis of physical considerations it is argued that the ballooning-mode type description is comparatively the most accurate and complete description of plasma instability in the equatorial ionosphere where the inhomogeneous plasma is embedded in a dipole magnetic field. The growth rates obtained from the ballooning-mode type description are therefore the most accurate growth rates. In comparison, the local description overestimates the growth rates up to a certain altitude and then underestimates them, while the flux tube integrated description underestimates the growth rates at almost all altitudes where the growth rates are significant. This is shown for two sets of ionospheric plasma conditions. It is further pointed out that only the ballooning-mode type description provides useful information on the wavelength dependence of the growth rates as well as on the spatial profiles of the excited modes. The localized spatial structures of the linear modes along the magnetic field line that are found in the ballooning-mode type description are expected to impose topological constraints on the nonlinear evolution of the instability and thus to play an important role in the determination of the nonlinear state of the plasma.

**15. SUBJECT TERMS**

Equatorial ionosphere  
Irregularities

Plasma instability  
Growth rates

Density  
Flux tubes

**16. SECURITY CLASSIFICATION OF:**

a. REPORT  
UNCLAS

UNCLAS

c. THIS PAGE  
UNCLAS

**17. LIMITATION  
OF ABSTRACT**

SAR

**18. NUMBER  
OF PAGES**

10

**19a. NAME OF RESPONSIBLE PERSON**

B. Basu

**19b. TELEPHONE NUMBER (include area  
code)**

781-377-3048

Standard Form 298 (Rev. 8-98)  
Prescribed by ANSI Std. Z39.18

Best Available Copy

## On the linear theory of equatorial plasma instability: Comparison of different descriptions

B. Basu

Air Force Research Laboratory, Space Vehicles Directorate, Hanscom Air Force Base, Massachusetts, USA

Received 26 September 2001; revised 12 November 2001; accepted 13 November 2001; published 22 August 2002.

[1] Three theoretical descriptions, namely, the local description, the flux tube integrated description and the ballooning-mode type description, of the equatorial plasma instability are presented for comparisons. On the basis of physical considerations it is argued that the ballooning-mode type description is comparatively the most accurate and complete description of plasma instability in the equatorial ionosphere where the inhomogeneous plasma is embedded in a dipole magnetic field. The growth rates obtained from the ballooning-mode type description are therefore the most accurate growth rates. In comparison, the local description overestimates the growth rates up to a certain altitude and then underestimates them, while the flux tube integrated description underestimates the growth rates at almost all altitudes where the growth rates are significant. This is shown for two sets of ionospheric plasma conditions. It is further pointed out that only the ballooning-mode type description provides useful information on the wavelength dependence of the growth rates as well as on the spatial profiles of the excited modes. The localized spatial structures of the linear modes along the magnetic field line that are found in the ballooning-mode type description are expected to impose topological constraints on the nonlinear evolution of the instability and thus to play an important role in the determination of the nonlinear state of the plasma.

**INDEX TERMS:** 2415 Ionosphere: Equatorial ionosphere; 2439 Ionosphere: Ionospheric irregularities; 2471 Ionosphere: Plasma waves and instabilities; 2437 Ionosphere: Ionospheric dynamics; **KEYWORDS:** equatorial ionosphere, plasma instability, density irregularities, growth rates, flux tube

### 1. Introduction

[2] The theoretical as well as the practical importance of equatorial plasma instability, which is driven by the combined effects of gravity, eastward electric field, and vertically downward neutral wind in the presence of a vertically upward density gradient, is now well recognized. The instability generates density fluctuations (irregularities) in the *F* region ionosphere after sunset, and these density irregularities are commonly referred to as the equatorial spread *F* (ESF). The practical importance of the instability lies in the fact that in the nonlinear stage of its evolution it can result in the formation of the so-called "bubbles" and "plumes," which are large-scale density-depleted structures that cause scintillation of the radio signals used in communication and navigation systems. Although the plasma instability and its consequences are usually observed in the fully developed nonlinear state so that a nonlinear theory is needed to explain the observations, the linear theory is useful for understanding the basic physical mechanism of the instability and the characteristics of the excited plasma modes. In addition, the growth rates obtained from the linear theory can be used to specify/predict the region of the equatorial ionosphere where bubbles and plumes may be

expected and thus can be of importance to a space weather specification/forecasting scheme. Thus, for a better understanding of the instability process as well as for an accurate calculation of the growth rates, it is essential that a physically accurate description of the linear stage of the instability be adopted.

[3] There are three theoretical descriptions of the instability that are found in the literature. Among them, the most elementary description [see e.g., Kelley, 1989] assumes flute type perturbations meaning  $\mathbf{k} \cdot \mathbf{B}_0 = 0$ , where  $\mathbf{k}$  is the wave vector and  $\mathbf{B}_0$  is the magnetic field, which is taken to be uniform. In other words, this description neglects the parallel (to  $\mathbf{B}_0$ ) dynamics of electrons and ions in the plasma. Furthermore, it makes the so-called local approximation in treating the plasma inhomogeneity along the vertical direction and calculates the growth rate by using the local value of the vertical density gradient at the magnetic equator (say). The local approximation imposes a restrictive condition on the perpendicular wavelengths of the excited modes; namely, the wavelengths must be small compared to the scale length of the vertical density gradient. The above conditions are, in fact, the limiting conditions under which the classical interchange instability is realized. In the equatorial *F* region, where the ion-neutral collisions dominate over the inertial effects, the instability is termed as the collisional interchange instability and is also referred to as the generalized Rayleigh-Taylor insta-

bility. In reality, the flute-type perturbations are not consistent with the experimental observation, which indicates that the unstable perturbations are extended along the magnetic field line and that the plasma along almost the entire field line participates in the instability process. This is an issue of particular importance in the study of the equatorial plasma instability, since the plasma is spatially nonuniform along the curved dipole magnetic field line and since, as is well known in plasma physics, such spatial inhomogeneity can have significant effect on both the topology and the growth rate of the excited modes. In an effort to include the effects of plasma inhomogeneity along the field line, G. Haerendel (Theory of equatorial spread  $F$ , preprint, 1973, hereinafter referred to as Haerendel, preprint, 1973) introduced the flux tube integrated description. In this description the plasma equations are first integrated along the field line and then analyzed to obtain the growth rates of the unstable perturbations. Consequently, the effects of plasma inhomogeneity along the field line are taken into account only in a gross manner. Besides, the flux tube integration is made possible by assuming that the field lines are equipotentials. The equipotential assumption can be justified if the parallel electrical conductivity is extremely large everywhere along the field line. In reality, the parallel conductivity may be large near the equator at  $F$  region altitudes, but away from the equator it decreases rapidly as the dipole field line bends into the lower-altitude regions. As a result, the equipotential assumption breaks down. In fact, the finite parallel electric field that is sustained along the curved field line due to finite resistivity can significantly influence the excitation of the unstable plasma modes. The ballooning-mode type description [Basu and Coppi, 1983, 1984; Basu, 1998] avoids the equipotential assumption. Instead, it allows for the variation of perturbed density and electrostatic potential along the dipole magnetic field line in recognition of the finite electrical resistivity and determines growth rates by solving the differential equation that describes the variation of the perturbation amplitudes. Thus it includes the full impact of the spatial inhomogeneity, including that of the parallel electric field, on the growth rates. So, on the basis of physical considerations alone it may be argued that the ballooning-mode type description is comparatively the most accurate description of the plasma instability in the equatorial ionosphere where the inhomogeneous plasma is embedded in a dipole magnetic field. The growth rates obtained from this description should therefore be the most accurate growth rates. The spatially localized plasma modes, which are found in this description and which are made possible by the sharp increase of plasma resistivity along the curved magnetic field line, are topologically similar to the so-called ballooning modes [Coppi *et al.*, 1979], although the excitation mechanism is different. The purpose of this paper is to present quantitative comparisons of the growth rates obtained from the three theoretical descriptions and to point out other significant differences.

[4] Although the theoretical formulations of the three descriptions can be found in the published literature, we repeat them in sections 2 and 3 for the sake of completeness and for convenience of comparisons. In doing so, we believe that we have improved upon the earlier presentations. The quantitative comparisons are presented in section 4.

The paper is concluded with a summary and discussion in section 5.

## 2. Plasma Model

[5] The collisional plasma instability in the nighttime equatorial ionosphere is described by the particle (electron) conservation equation

$$\frac{\partial n}{\partial t} + \nabla \cdot (n \mathbf{V}_e) = -R \quad (1)$$

and the charge conservation equation

$$\nabla \cdot \mathbf{j} \equiv e \nabla \cdot [n(\mathbf{V}_i - \mathbf{V}_e)] = 0, \quad (2)$$

where  $n$  is the particle density,  $R$  is the rate of change of particle density due to recombination process,  $\mathbf{j}$  is the current density, and the quasi-neutrality condition ( $n_e = n_i = n$ ) is assumed. The flow velocities  $\mathbf{V}_e$  and  $\mathbf{V}_i$ , where the subscripts  $e$  and  $i$  refer to electrons and ions, respectively, are determined from the momentum balance equations

$$0 = -e(\mathbf{E} + \frac{1}{c} \mathbf{V}_e \times \mathbf{B}_0) - m_e \nu_{ei}(\mathbf{V}_e - \mathbf{V}_i) - m_e \nu_{en}(\mathbf{V}_e - \mathbf{V}_n) + m_e \mathbf{g}, \quad (3)$$

$$0 = e(\mathbf{E} + \frac{1}{c} \mathbf{V}_i \times \mathbf{B}_0) + m_e \nu_{ei}(\mathbf{V}_e - \mathbf{V}_i) - m_i \nu_{in}(\mathbf{V}_i - \mathbf{V}_n) + m_i \mathbf{g}, \quad (4)$$

where  $\nu_{en}$  is the electron-neutral collision frequency,  $\nu_{ei}$  is the electron-ion collision frequency,  $\nu_{in}$  is the ion-neutral collision frequency,  $\mathbf{g}$  is the acceleration due to gravity,  $\mathbf{V}_n$  is the neutral wind velocity, and the other quantities have their standard meanings. The inertia terms in the momentum balance equations have been ignored since the growth rate  $\gamma$  of the instability satisfies the inequality  $\gamma \ll (\nu_{in}, \nu_{en}, \nu_{ei})$  in the altitude region of interest. The pressure gradient terms have small effects on the evolution of the ambient plasma but can have significant damping effects on the excited plasma modes if the wavelengths of the modes are shorter than  $\sim 100$  m. However, they are neglected in this paper since longer wavelength modes will be considered.

[6] In the altitude range of our interest,  $(\nu_{en}/\Omega_e)$ ,  $(\nu_{ei}/\Omega_e) \ll 1$ , but  $(\nu_{in}/\Omega_i)$  can vary from being larger than unity (in the  $E$  region) to being much less than unity (in the  $F$  region). Here the  $\Omega$  values are the cyclotron frequencies. So, neglecting terms of the order of  $(\nu_{en}/\Omega_e)$ ,  $(\nu_{ei}/\Omega_e)$ ,  $(m_e \nu_{en})/(m_i \nu_{in})$ ,  $\mathbf{g}/\Omega_e$  and smaller, but retaining  $(\nu_{in}/\Omega_i)$  to all orders, we find from equations (3) and (4)

$$\mathbf{V}_e = \frac{c}{B_0^2} \mathbf{E} \times \mathbf{B}_0 - \frac{e \mathbf{E}_{\parallel}}{m_e \nu_e} + \left(1 + \frac{\nu_{ei}}{\nu_{in}}\right) \frac{\mathbf{g}_{\parallel}}{\nu_e} + \mathbf{V}_{n\parallel}, \quad (5)$$

$$\mathbf{V}_i = \frac{1}{1 + \nu_{in}^2/\Omega_i^2} \left[ \frac{c}{B_0^2} \mathbf{E} \times \mathbf{B}_0 + \frac{1}{\Omega_i B_0} \hat{\mathbf{g}} \times \mathbf{B}_0 + \frac{\nu_{in}}{\Omega_i} \left( \frac{c}{B_0} \mathbf{E}_{\perp} + \frac{1}{\Omega_i} \hat{\mathbf{g}}_{\perp} \right) \right] + \frac{\hat{\mathbf{g}}_{\parallel}}{\nu_{in}}. \quad (6)$$

Here  $\nu_e = \nu_{ei} + \nu_{en}$ ,  $\hat{\mathbf{g}} = \mathbf{g} + \nu_{in} \mathbf{V}_n$ , and the subscripts  $\parallel$  and  $\perp$  denote parallel and perpendicular (to  $\mathbf{B}_0$ ) components,

respectively. The current density  $\mathbf{j}$  calculated from equations (5) and (6) can be written as

$$\mathbf{j} = \sigma_P \left( \mathbf{E}_\perp + \frac{\hat{\mathbf{g}} \times \mathbf{B}_0}{c v_{in}} \right) - \sigma_H \left( \frac{\mathbf{E} \times \mathbf{B}_0}{B_0} - \frac{B_0}{c v_{in}} \hat{\mathbf{g}}_\perp \right) + \sigma_\parallel \mathbf{E}_\parallel + \frac{en}{v_e} \left( \frac{v_{en}}{v_{in}} - 1 \right) \mathbf{g}_\parallel, \quad (7)$$

where

$$\sigma_P = \frac{enc}{B_0} \frac{v_{in}/\Omega_i}{1 + v_{in}^2/\Omega_i^2} \quad (8)$$

$$\sigma_H = \frac{enc}{B_0} \frac{v_{in}^2/\Omega_i^2}{1 + v_{in}^2/\Omega_i^2} = \frac{v_{in}}{\Omega_i} \sigma_P \quad (9)$$

$$\sigma_\parallel = \frac{e^2 n}{m_e v_e} \quad (10)$$

are the Pedersen, Hall, and parallel (specific) conductivities, respectively.

### 3. Linear Stability Analysis

[7] The linear stability analysis is performed by considering small-amplitude perturbations (denoted by subscript 1) from the equilibrium state (denoted by subscript 0) and by solving the first-order, linearized equations

$$\frac{\partial n_1}{\partial t} + \nabla \cdot (n_0 \mathbf{V}_{e1} + n_1 \mathbf{V}_{e0}) = 0, \quad (11)$$

$$\nabla \cdot \mathbf{j}_1 = 0, \quad (12)$$

where  $\mathbf{V}_{e0} \cong c(\mathbf{E}_0 \times \mathbf{B}_0)/B_0^2$  and

$$\mathbf{V}_{e1} = \frac{c}{B_0^2} \mathbf{E}_1 \times \mathbf{B}_0 - \frac{e \mathbf{E}_{1\parallel}}{m_e v_e} \quad (13)$$

$$\mathbf{j}_1 = \sigma_{P0} \mathbf{E}_{1\perp} - \sigma_{H0} \left( \frac{\mathbf{E}_1 \times \mathbf{B}_0}{B_0} + \sigma_{\parallel 0} \mathbf{E}_{1\parallel} + \mathbf{j}_0 \frac{n_1}{n_0} \right) \quad (14)$$

with

$$\mathbf{j}_0 = \sigma_{P0} \left( \mathbf{E}_{0\perp} + \frac{\hat{\mathbf{g}} \times \mathbf{B}_0}{c v_{in}} \right) - \sigma_{H0} \left( \frac{\mathbf{E}_0 \times \mathbf{B}_0}{B_0} - \frac{B_0}{c v_{in}} \hat{\mathbf{g}}_\perp \right) + \mathbf{j}_{0\parallel}. \quad (15)$$

The recombination loss term has been omitted in equation (11) for the following reason. The plasma instability occurs primarily in the  $F$  region where the recombination loss term is  $v_R n$ ,  $v_R$  being the recombination frequency. If  $v_R$  is taken to be spatially uniform, then it can be shown that the time evolution of  $n_1/n_0$  is unaffected by the recombination loss [Huba *et al.*, 1996; Basu, 1997]. It is true, as shown in sections 3.2 and 3.3, that there are some contributions to the instability from the plasma in the  $E$  region, where the recombination loss is  $\propto n^2$  and thus introduces some damping of  $n_1/n_0$  locally. However, this damping contribu-

tion to the overall growth of the instability is very small and can be neglected. The recombination loss term, however, plays an important role in determining the equilibrium plasma state from the zero-order form of equation (1), when the ambient fields  $\mathbf{E}_0$ ,  $\mathbf{B}_0$ , and the neutral wind velocity  $\mathbf{V}_n$  are specified.

#### 3.1. Local Description (Collisional Interchange Instability)

[8] Neglecting the parallel (to  $\mathbf{B}_0$ ) components of  $\mathbf{V}_{e1}$  and  $\mathbf{j}_1$ , and considering electrostatic modes so that  $\mathbf{E}_1 = -\nabla_\perp \phi_1$ , where  $\phi_1$  is the electrostatic potential, we find from equations (11) and (12) that

$$\left( \frac{\partial}{\partial t} + \mathbf{V}_{e0} \cdot \nabla_\perp \right) n_1 = -\frac{c}{B_0^2} (\mathbf{B}_0 \times \nabla_\perp \phi_1) \cdot \nabla_\perp n_0, \quad (16)$$

$$\left[ \nabla_\perp^2 + \frac{\sigma_{H0}}{\sigma_{P0}} \frac{1}{n_0 B_0} \nabla_\perp n_0 \cdot (\mathbf{B}_0 \times \nabla_\perp) \right] \phi_1 = \frac{1}{\sigma_{P0} n_0} \mathbf{j}_0 \cdot \nabla_\perp n_1, \quad (17)$$

where the local approximation  $\nabla_\perp^2 \gg (\nabla_\perp n_0/n_0) \cdot \nabla_\perp$  has been made and the spatial variation of  $v_{in}$  has been neglected. Next, considering the perturbed quantities to vary as  $\sim \exp(\gamma t + i \mathbf{k}_\perp \cdot \mathbf{r}_\perp)$ , using  $(\sigma_{H0}/\sigma_{P0})[(\mathbf{k}_\perp \times \mathbf{B}_0) \cdot \nabla_\perp n_0]/(n_0 B_0) \ll k_\perp^2$  and combining equations (16) and (17), we obtain the local dispersion relation

$$\gamma + i \mathbf{k}_\perp \cdot \mathbf{V}_{e0} = \frac{(\mathbf{k}_\perp \times \mathbf{B}_0) \cdot \nabla_\perp n_0}{n_0 B_0 k_\perp^2} \left[ \mathbf{k}_\perp \cdot \left( \frac{c}{B_0} \mathbf{E}_{0\perp} + \frac{\hat{\mathbf{g}} \times \mathbf{B}_0}{v_{in} B_0} + \frac{\sigma_{H0}}{\sigma_{P0}} \frac{\hat{\mathbf{g}}_\perp}{v_{in}} \right) \right]. \quad (18)$$

Applying this result to the magnetic equator, where  $\nabla n_0 > 0$  and  $\mathbf{g} < 0$  in the upward direction (taken to be the  $x$  direction of a Cartesian coordinate system),  $\mathbf{B}_0$  is northward ( $z$  direction), and choosing  $\mathbf{E}_0$  and  $\mathbf{k}_\perp$  to be in the eastward direction ( $y$  direction), the explicit expression for the growth rate is found to be

$$\gamma = \frac{1}{L_n} \left( \frac{g}{v_{in}} + \frac{c E_{0y}}{B_0} - V_{nx} + \frac{v_{in}}{\Omega_i} V_{ny} \right), \quad (19)$$

which is independent of  $k_\perp$ . Here  $1/L_n = d \ln n_0 / dx$ . A positive definite growth rate is obtained when  $E_{0y} > 0$ ,  $V_{nx} < 0$  and  $V_{ny} > 0$ . This is a well-known result for collisional interchange instability (also referred to as generalized Rayleigh-Taylor instability) that includes not only the effects of gravity and ambient electric field but also those of both the zonal and the vertical components of the neutral wind velocity [see, e.g., Kelley, 1989].

#### 3.2. Flux Tube Integrated Description

[9] In the flux tube integrated description, introduced by Haerendel (preprint, 1973), the particle and charge conservation equations are first integrated along the magnetic field with the assumption that the field lines are equipotentials. The perturbation analysis is then applied to the integrated equations to determine the instability. The details of the derivation of those equations can be found in the work of Haerendel (preprint, 1973) and Haerendel *et al.* [1992]. Here we briefly outline the procedure and present the results.



[10] Before integrating, the particle flux and the current density are expressed in the local dipole coordinate system  $(\rho, \psi, s)$  with unit vectors  $\mathbf{e}_\rho, \mathbf{e}_\psi, \mathbf{e}_s$  where  $\mathbf{e}_\rho$  is perpendicular to  $\mathbf{B}_0 (= B_0 \mathbf{e}_s)$  and lies in the meridian plane pointing upward and  $\mathbf{e}_\psi = \mathbf{e}_s \times \mathbf{e}_\rho$ . The dipole coordinate system can be defined in terms of the spherical coordinate system  $(r, \psi, \theta)$ , with unit vectors  $\mathbf{e}_r, \mathbf{e}_\psi, \mathbf{e}_\theta$  as

$$\rho = \frac{r}{\cos^2 \theta}, \quad s = \frac{r_0^2}{r^2} \sin \theta, \quad (20)$$

where  $\theta$  being measured from the equatorial plane is the magnetic latitude and  $r_0$  is the radial distance from the Earth's center at which a field line intersects the equatorial plane. The equation for a field line that intersects the equatorial plane at  $r = r_0$  is  $r = r_0 \cos^2 \theta$  and  $\mathbf{B}_0$  is represented by  $\mathbf{B}_0 = \bar{B}_0 (r_0/r)^3 (-2 \sin \theta \mathbf{e}_r + \cos \theta \mathbf{e}_\theta) \equiv B_{0r} \mathbf{e}_r + B_{0\theta} \mathbf{e}_\theta$ , so that  $B_0 = \bar{B}_0 (r_0/r)^3 (1 + 3 \sin^2 \theta)^{1/2}$  and  $\bar{B}_0 = B_0 (r = r_0, \theta = 0)$ . The unit vectors in the two coordinate systems are related by  $\mathbf{e}_\rho = (B_{0\theta}/B_0) \mathbf{e}_r - (B_{0r}/B_0) \mathbf{e}_\theta$ ,  $\mathbf{e}_\psi = (B_{0r}/B_0) \mathbf{e}_r + (B_{0\theta}/B_0) \mathbf{e}_\theta$ , and  $\mathbf{e}_s = \mathbf{e}_\psi$ . Furthermore, the scale factors  $(h_\rho, h_\psi, h_s)$ , which describe the magnetic field geometry, are

$$h_\rho = \frac{\cos^3 \theta}{(1 + 3 \sin^2 \theta)^{1/2}}, \quad h_\psi = r \cos \theta, \quad h_s = \frac{(r/r_0)^3}{(1 + 3 \sin^2 \theta)^{1/2}} \equiv \frac{\bar{B}_0}{B_0}. \quad (21)$$

The flux tube integrated transverse particle flux and current density are then expressed in the two-dimensional  $(L, \varphi)$  coordinate system placed in the equatorial plane, after relating the fields and quantities in the local  $(\rho, \psi, s)$  coordinate system to the fields and quantities in the  $(L, \varphi)$  coordinate system. Here  $L$  is the McIlwain parameter defined by  $r_0 = R_E L$  ( $R_E$  is the radius of Earth) and  $\varphi$  is the geomagnetic longitude. The resulting integrated equations are

$$\frac{\partial N}{\partial t} + \nabla_\perp \cdot \mathbf{F}_\perp = 0, \quad (22)$$

$$\nabla_\perp \cdot \mathbf{J}_\perp = 0, \quad (23)$$

where  $N$  is the flux tube content of the number density,  $\mathbf{F}_\perp$  and  $\mathbf{J}_\perp$  are the flux tube integrated transverse electron flux and current density, respectively, and  $\nabla_\perp$  is the field line integrated transverse divergence operator defined as

$$\nabla_\perp \cdot \mathbf{A}_\perp = \frac{1}{R_E L} \left[ \frac{\partial}{\partial L} (L A_L) + \frac{\partial}{\partial \varphi} A_\varphi \right]. \quad (24)$$

Using  $\mathbf{V}_{e\perp}$  given by equation (5), and following Haerendel (preprint, 1973) and Haerendel *et al.* [1992] we find

$$F_L = \frac{c E_\varphi}{\bar{B}_0 N} \quad (25)$$

$$F_\varphi = -\frac{c E_L}{\bar{B}_0} N. \quad (26)$$

Here  $\bar{B}_0$  is the equatorial value of the magnetic field strength at the location of the field line so that  $\bar{B}_0 = \hat{B}^0/L^3$ ,

where  $\hat{B}_0$  is the value on Earth's surface ( $L = 1$ ), and  $N$  is given by

$$N = R_E L \int n (1 - \zeta^2)^3 d\zeta \quad (27)$$

with  $\zeta = \sin \theta$ . Similarly, from  $\mathbf{j}_\perp$  given by equation (7) we obtain

$$J_L = \Sigma_P E_L - \Sigma_H E_\varphi + \frac{\bar{B}_0}{c} (\Sigma_P U_\varphi^P + \Sigma_H U_L^H) - \frac{\bar{B}_0 \bar{g}}{c} I_H^V \quad (28)$$

$$J_\varphi = \tilde{\Sigma}_P E_\varphi + \Sigma_H E_L - \frac{\bar{B}_0}{c} (\tilde{\Sigma}_P U_L^P - \Sigma_H U_\varphi^H) + \frac{\bar{B}_0 \bar{g}}{c} I_P^V. \quad (29)$$

Here  $\bar{g}$  is the equatorial value of the gravitational acceleration at the location of the field line so that  $\bar{g} = g_0/L^2$ , where  $g_0$  is the value on Earth's surface ( $L = 1$ ), and the following definitions have been used:

$$\Sigma_P = R_E L \int \sigma_P (1 + 3\zeta^2) d\zeta \quad (30)$$

$$\tilde{\Sigma}_P = R_E L \int \sigma_P d\zeta \quad (31)$$

$$\Sigma_H = R_E L \int \sigma_H (1 + 3\zeta^2)^{1/2} d\zeta \quad (32)$$

$$\Sigma_P U_\varphi^P = R_E L \int \sigma_P V_{n\psi} \frac{1 + 3\zeta^2}{(1 - \zeta^2)^{3/2}} d\zeta \quad (33)$$

$$\tilde{\Sigma}_P U_L^P = R_E L \int \sigma_P V_{n\psi} \frac{(1 + 3\zeta^2)^{1/2}}{(1 - \zeta^2)^{3/2}} d\zeta \quad (34)$$

$$\Sigma_H U_L^H = R_E L \int \sigma_H V_{n\psi} \frac{1 + 3\zeta^2}{(1 - \zeta^2)^{3/2}} d\zeta \quad (35)$$

$$\Sigma_H U_\varphi^H = R_E L \int \sigma_H V_{n\psi} \frac{(1 + 3\zeta^2)^{1/2}}{(1 - \zeta^2)^{3/2}} d\zeta \quad (36)$$

$$I_P^V = R_E L \int \frac{\sigma_P}{v_{in} (1 - \zeta^2)^3} d\zeta \quad (37)$$

$$I_H^V = R_E L \int \frac{\sigma_H}{v_{in}} \frac{(1 + 3\zeta^2)^{1/2}}{(1 - \zeta^2)^3} d\zeta. \quad (38)$$

These definitions, with the exception of the last two, are the same as those of Haerendel (preprint, 1973) and Haerendel *et al.* [1992].

[11] Considering  $N = N_0 + N_1$ ,  $\mathbf{E}_\perp = \mathbf{E}_{0\perp} - \nabla_\perp \phi_1$  where  $\mathbf{E}_{0\perp} = E_{0\varphi} \mathbf{e}_\varphi$  and where the small amplitude perturbations  $N_1$  and  $\phi_1$  are assumed to have the space-time dependence of the form  $f_1(L, \varphi, t) = \tilde{f}_1(L = L_0) \exp(\gamma t + im\varphi)$  (i.e., the  $L$  dependence of the perturbations is treated locally), one can derive the complete dispersion relation by combining the linearized versions of equations (22) and (23). However, it is recognized that  $\Sigma_{P0} \gg \Sigma_{H0}/m$  and

$\tilde{\Sigma}_{P0} \gg (L/m)(\partial \Sigma_{H0}/\partial L)$ , as  $k_p R_E \gg k_p L_N (v_{in}/\Omega_i)$ . Then, keeping only the significant leading order terms we obtain a more useful linear dispersion relation

$$\gamma = \frac{\bar{g}}{L_N} \frac{I_{P0}^r}{\Sigma_{P0}} + \frac{1}{L_N} \left( \frac{cE_{0\phi}}{B_0} + \frac{\Sigma_{H0}}{\Sigma_{P0}} U_\phi^H - U_L^P \right), \quad (39)$$

which closely resembles the form of the local expression (19). In the above,  $L_N$  is the scale length of the gradient of the flux tube integrated density, evaluated locally at  $L = L_0$  and defined by

$$\frac{1}{L_N} = \frac{1}{R_E} \frac{d}{dL} \ln(L^3 N_0) \quad (40)$$

and the flux tube integrated quantities with subscript 0 are the unperturbed values of the same. A similar dispersion relation was presented earlier by Sultan [1996], although his notations are different from ours. Haerendel's (preprint, 1973) expression for the growth rate does not include the effects of eastward electric field and neutral wind. Both Haerendel (preprint, 1973) and Sultan [1996] omitted the factor  $1/(1 + v_{in}^2/\Omega_i^2)$  in the gravitational term of  $J_\phi$ . This factor starts to deviate from unity below 150 km and should be included in order to get a more accurate value of the integrated quantity. In our presentation it is included in  $I_P^r$ , which has been defined in such a way that the gravitational term in  $\gamma$  can be immediately recognized to be of the form:  $\bar{g}/v_{in}^{eff} L_N$ . It is clear that the growth rate given by equation (39) is different from the local growth rate equation (19), since the integrated quantities  $L_N$ ,  $(I_{P0}^r/\Sigma_{P0})$ ,  $(\Sigma_{H0}/\Sigma_{P0}) U_\phi^H$  and  $U_L^P$  are different from the corresponding local values. We also note that to this lowest significant order of analysis, the flux tube integrated growth rate, like the local growth rate, is independent of wavelength.

### 3.3. Ballooning-Mode Type Description

[12] In this description the equipotential assumption is discarded and the plasma inhomogeneity along the magnetic field is treated rigorously by retaining the parallel dynamics in the analysis.

[13] We refer to the dipole coordinate system described in the previous section and consider an equilibrium plasma state described by  $n_0 = n_0(\rho, s)$ ,  $\mathbf{E}_0 = E_{0\psi} \mathbf{e}_\psi$ , and  $\mathbf{g} = -g \mathbf{e}_r$ . The equilibrium density distribution is determined from the conservation equations when the zero-order (ambient) electric fields and neutral wind velocities are specified. The stability of small-amplitude perturbations is studied by retaining the parallel components of  $\mathbf{V}_{e1}$  and  $\mathbf{j}_1$ . As before, electrostatic perturbation is considered and the perturbed quantities are assumed to have space-time dependence of the form  $\mathbf{A}_1(\rho, \psi, s, t) = \tilde{\mathbf{A}}_1(\rho = \rho_0, s) \exp(\gamma t + im\psi)$ , so that the  $\rho$ -dependence of the perturbations is treated locally. Substituting for  $\mathbf{V}_{e1}$  in equation (11), we find

$$\gamma \frac{n_1}{n_0} = \frac{im}{h_p h_\psi} \left( \frac{\partial \ln n_0}{\partial \rho} \right) \frac{c\phi_1}{B_0} - \frac{1}{en_0 h_p h_\psi h_s} \frac{\partial}{\partial s} \left( \sigma_{\parallel 0} \frac{h_p h_\psi}{h_s} \frac{\partial \phi_1}{\partial s} \right). \quad (41)$$

Also, substituting for  $\mathbf{j}_1$  in equation (12) and neglecting the altitude variation of  $v_{in}$  compared to that of  $n_0$ , we find

$$\begin{aligned} \frac{\partial}{\partial s} \left( \sigma_{\parallel 0} \frac{h_p h_\psi}{h_s} \frac{\partial \phi_1}{\partial s} \right) - m^2 \sigma_{P0} \frac{h_p h_s}{h_\psi} \left( 1 + \frac{i}{m} \frac{h_\psi}{h_p} \frac{\sigma_{H0}}{\sigma_{P0}} \frac{\partial \ln n_0}{\partial \rho} \right) \tilde{\phi}_1 \\ = \left( im h_p h_s j_{0\psi} + h_p h_\psi j_{0\parallel} \right) \frac{\partial}{\partial s} \tilde{n}_1. \end{aligned} \quad (42)$$

At this point, we recall that the equation for a field line that intersects the equatorial plane at  $r = r_0$  is  $r = r_0 \cos^2 \theta$ , where  $|\theta| < (\pi/12)$  for the ionospheric altitudes involved. Furthermore, the excited modes are found to be localized along the field line with localization distances that correspond to even smaller values of  $|\theta|$ . Hence  $s \cong r_0 \theta$  and  $s/r_0 \ll 1$  may be used. Then it can be verified that  $h_p h_\psi/h_s \approx r_0$  to leading order and may be taken outside the derivatives in equations (41) and (42) without introducing any significant error. In addition, we assume that  $(h_\psi/m h_p)(\sigma_{H0}/\sigma_{P0})(\partial \ln n_0/\partial \rho) \approx (r_0/m)(1/L_N)(v_{in}/\Omega_i) \ll 1$ , where  $L_N \equiv h_p/(\partial \ln n_0/\partial \rho)$ . This condition implies that  $k_\psi L_N \gg (v_{in}/\Omega_i)$ , where  $k_\psi (= m/r_0)$  represents the longitudinal wave number, and it is easily satisfied. Then, combining equations (41) and (42) and using the expression for  $j_{0\psi}$  while neglecting  $j_{0\parallel}$  in comparison, we obtain a second-order differential equation that describes the spatial profile (along  $\mathbf{B}_0$ ) of the normal modes. The differential equation is

$$\begin{aligned} \left( \gamma + \frac{im}{h_\psi} V_{i0\psi} \right) \frac{1}{\sigma_{\parallel 0}} \frac{\partial}{\partial s} \left( \sigma_{\parallel 0} \frac{\partial \tilde{\phi}_1}{\partial s} \right) - k_\psi^2 f(s) R(s) \\ \cdot \left\{ \gamma - \frac{1}{L_N} \left[ V_{0p} - \frac{1}{v_{in}} \left( \hat{g}_\rho - \frac{v_{in}}{\Omega_i} \hat{g}_\psi \right) \right] \right\} \tilde{\phi}_1 = 0, \end{aligned} \quad (43)$$

where  $V_{0p} = cE_{0\psi}/B_0$ ,  $f(s) = h_s^2 r_0^2/h_\psi^2$ ,  $R(s) = \sigma_{P0}/\sigma_{\parallel 0} = [(v_e v_{in})/[(v_e v_{in})/(\Omega_e \Omega_i)]/(1 + v_{in}^2/\Omega_i^2)]$ , and

$$V_{i0\psi} = \frac{1}{1 + v_{in}^2/\Omega_i^2} \left[ -\frac{\hat{g}_\rho}{\Omega_i} + \frac{v_{in}}{\Omega_i} \left( V_{0p} + \frac{\hat{g}_\psi}{\Omega_i} \right) \right]. \quad (44)$$

For the purpose of this paper, we ignore the imaginary term in equation (43) and consider instead the simplified form

$$\begin{aligned} \frac{1}{\sigma_{\parallel 0}} \frac{\partial}{\partial s} \left( \sigma_{\parallel 0} \frac{\partial \tilde{\phi}_1}{\partial s} \right) - k_\psi^2 f(s) R(s) \\ \cdot \left\{ 1 - \frac{1}{\gamma L_N} \left[ V_{0p} - \frac{1}{v_{in}} \left( \hat{g}_\rho - \frac{v_{in}}{\Omega_i} \hat{g}_\psi \right) \right] \right\} \tilde{\phi}_1 = 0. \end{aligned} \quad (45)$$

Equation (45) is an eigenvalue equation in which the eigenvalue  $\gamma$  (the growth rate) is determined by requiring that the eigenfunction  $\phi_1$  be bounded at large value of  $|s|$ . The numerical procedure finds a solution of the equation for a given value of  $\gamma$  and then  $\gamma$  is varied until the required well-behaved solution with  $\phi_1 \rightarrow 0$  and  $\partial \phi_1/\partial s \rightarrow 0$  at large value of  $|s|$  is achieved. The spatially bounded solutions of  $\phi_1$  are made possible primarily due to the sharp increase of  $R(s)$  along the curved magnetic field line. One immediate distinction between the ballooning-mode description and the other two descriptions, which can be observed from equation (45), is that the spatial profiles of the excited modes as well

as the growth rates depend on the wavelength  $\lambda_\psi (\equiv 2\pi/k_\psi)$  explicitly.

[14] The numerical solutions of equation (45) are presented in the next section. Here we consider a heuristic analysis. We ignore the  $s$ -variation of all the equilibrium plasma parameters, consider instead their values at  $s = s_0 = 0$  (say), and replace  $\partial/\partial s$  by  $ik_\parallel$ . The differential equation is thus reduced to an algebraic equation for  $\phi_1$ . The nontrivial solution of the equation determines  $\gamma$ , which is

$$\gamma = \frac{1}{L_n} \left( \frac{g}{v_{in}} + \frac{cE_{0\psi}}{B_0} - V_{np} + \frac{v_{in}}{\Omega_i} V_{m\psi} \right) \left[ \frac{R(0)}{R(0) + k_\parallel^2/k_\psi^2} \right]. \quad (46)$$

Comparison with equation (19) shows that this growth rate is smaller than the local growth rate by the factor  $R(0)/[R(0) + k_\parallel^2/k_\psi^2]$ . To have an estimate of this factor, we consider  $k_\parallel \geq \pi/2l$  in order to simulate the boundary condition of the problem, where  $2l$  is the length of a field line, and take  $l \sim 1.5 \times 10^3$  km,  $R(0) \sim 10^{-7}$  as the typical values of the parameters in the bottomside of  $F$  region. Then,  $k_\parallel^2/k_\psi^2$  is found to be either comparable to or larger than  $R(0)$  when  $\lambda_\psi$  (wavelength in the east-west direction)  $\geq 2$  km. So, the growth rates, given by equation (46), are much smaller than the local growth rates when  $\lambda_\psi \geq 2$  km. When  $\lambda_\psi \ll 2$  km so that  $k_\parallel^2/k_\psi^2 \ll R(0)$ , the growth rates approach the local growth rates. These conclusions are, of course, based on the heuristic analysis. Evaluation of  $\gamma$  from the numerical solution of equation (45) shows that the growth rate given by the ballooning-mode type description is significantly different from that given by the local description even when  $\lambda_\psi = 300$  m.

[15] Like the local and the flux tube integrated descriptions, the ballooning-mode type description presented here treats the effects of plasma inhomogeneity in the vertical direction locally. This has been done for the sake of comparisons. A more accurate description considers the variation of perturbation amplitudes along the vertical direction as well. When this is done, the growth rates are determined by an eigenvalue equation which, unlike equation (45), is a second-order partial differential equation in two-dimensional  $(\rho, s)$  space [see Basu, 1998].

#### 4. Numerical Results

[16] In this section, the growth rates obtained from the three theoretical descriptions, presented in the previous section, are numerically evaluated for comparisons. We use the symbols  $\gamma_L$ ,  $\gamma_F$ , and  $\gamma_B$ , respectively, to refer to the three growth rates. The required inputs to the calculations are the ambient electron density ( $n_0$ ), the scale length of density gradient ( $L_n$ ), and the collision frequencies ( $\nu_e$ ,  $\nu_{in}$ ) as a function of  $\zeta$  and  $s$ . We recall that the variable  $\zeta$  is related to the distance  $s$  along a field line by  $s \cong r_0 \zeta$ , as  $\zeta \ll 1$  in the altitude region of interest. In this paper,  $V_n$  is neglected for simplicity. The Parameterized Ionospheric Model (PIM) of Daniell *et al.* [1995] and the Mass Spectrometer Incoherent Scatter (MSIS) thermosphere model of Hedin [1987] are used to obtain the ambient electron density and the neutral densities as a function of altitude and latitude for the geophysical conditions of 21 June 2000 and 20 April 2001 in the early evening (1900 LT). These 2 days were chosen in order to study the plasma instability during solstice and equinox conditions, when distinctly different

vertical plasma drift velocities are observed [Fejer *et al.*, 1999].

[17] The calculations proceed in the following way. The outputs of PIM and MSIS-86 are used to generate the electron densities and the neutral densities along a given magnetic field line whose apex altitude (the altitude at which the field line intersects the equatorial plane) is, say,  $h_0 (\equiv r_0 - R_E)$ . Using the electron and the neutral densities,  $\nu_e (= \nu_{ei} + \nu_{en})$ ,  $\nu_{in}$  and the various conductivities along the field line are then evaluated. For the purposes of this paper, the following formulae [Kelley, 1989; Schunk and Nagy, 1980], which are quite useful for quick estimates of the collision frequencies, are used:

$$\nu_{en} \cong (5.4 \times 10^{-10}) n_n T_e^{1/2} \quad (47)$$

$$\nu_{ei} \cong 54.5 n_0 / T_e^{3/2} \quad (48)$$

$$\nu_{in} \cong (2.6 \times 10^{-9}) n_n / M^{1/2}. \quad (49)$$

More rigorous expressions for the collision frequencies can be found in the work of Schunk and Nagy [1980], for example, and should be used in more accurate modeling studies. In the above expressions,  $n_n$  is the total neutral density in  $\text{cm}^{-3}$ ,  $n_0$  is the electron density in  $\text{cm}^{-3}$ ,  $T_e$  is the electron temperature in degrees Kelvin, and  $M$  is the mean molecular weight of the ions. We take  $T_e \approx T_n$  at night and at the altitudes of our interest, where  $T_n$  is the neutral temperature and is obtained from the MSIS-86 model. The single ion formulation adopted in this paper considers  $\text{O}^+$  to be the ion in the  $F$  region and  $\text{NO}^+$  and  $\text{O}_2^+$  lumped into one ion to be the ion in the  $E$  region. The dividing altitude between  $E$  and  $F$  regions is taken to be 160 km in order to be consistent with PIM. This is kept in mind when  $\nu_{in}$  and  $\Omega_i$  are calculated along the dipole field line. The values of the cyclotron frequencies ( $\Omega_e$  and  $\Omega_i$ ) are calculated with the help of  $B_0 = (\hat{B}_0/L^3)(1 + 3\zeta^2)^{1/2}/(1 - \zeta^2)^3$ , where  $\hat{B}_0 = 0.3$  G is chosen. The value of  $g_0$  is taken to be  $9.8 \text{ m/s}^2$ . The field line integrations in section 3.2 are carried out from  $\zeta = 0$  (the magnetic equator) to  $\zeta_{100}$  (value of  $\zeta$  at which the height of the field line is 100 km) and, for simplicity, the two hemispheres are assumed to be symmetric about the magnetic equator. The three growth rates ( $\gamma_L$ ,  $\gamma_F$ ,  $\gamma_B$ ) are then calculated using equations (19), (39), and (45), respectively. Finally, the above calculations are repeated for field lines with different values of  $h_0$ . The results are presented in Figures 1–6.

[18] The four panels in Figure 1 show the ionospheric parameters ( $n_0$ ,  $1/L_n$ ,  $\nu_{in}$  and  $\nu_e$ ) as a function of  $\hat{s} (\equiv s/l)$ , where  $2l$  is the length of the field line, for the geophysical conditions of 21 June 2000 at 1900 LT. The five curves in each panel are for five different field lines distinguished by their apex altitudes. These parameters are used in obtaining Figures 2 and 3. Figure 2 shows the growth rates obtained from the three descriptions as a function of the apex altitude  $h_0$ . The dashed curve represents the local growth rate  $\gamma_L$ , given by equation (19) and evaluated at the magnetic equator ( $\hat{s} = 0$ ). The dot-dashed curve represents the flux tube integrated growth rate  $\gamma_F$ , given by equation (39), while the four solid curves represent the growth rates  $\gamma_B$ , which are obtained from the solution of equation (45) for  $\lambda_\psi = 300$  m, 500 m, 1 km, and 2 km. The outermost solid curve is for  $\lambda_\psi =$

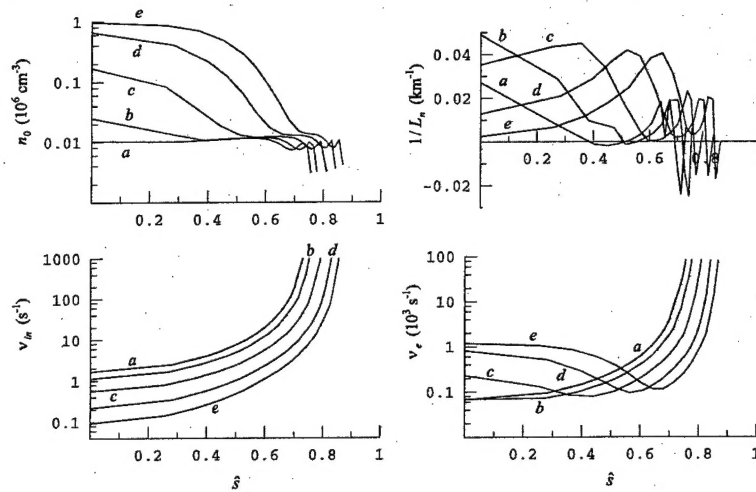


**Figure 1.** Profiles of the ionospheric parameters ( $n_0$ ,  $1/L_n$ ,  $\nu_{in}$  and  $\nu_e$ ) along a field line for the geophysical conditions on 21 June 2000 at 1900 LT. The labeled curves in each panel are for the field lines whose apex altitudes ( $h_0$ ) are (a) 240 km, (b) 260 km, (c) 300 km, (d) 360 km, and (e) 420 km.

300 m and the innermost is for  $\lambda_\psi = 2$  km, demonstrating that the growth rate decreases with increasing perpendicular (east-west direction) wavelength at all altitudes. Figure 2 shows that when compared to  $\gamma_B$ , the local description overestimates the growth rates up to a certain altitude and then underestimates them, while the flux tube integrated description underestimates the growth rates for  $\lambda_\psi \leq 1$  km at all altitudes above 240 km. For longer (than 1 km) wavelengths the flux tube integrated description and the ballooning-mode type description tend to yield similar growth rates at very low altitudes where the growth rates are small, but the difference persists at high altitudes. Earlier, *Rappaport* [1996] showed by means of a variational principle that the

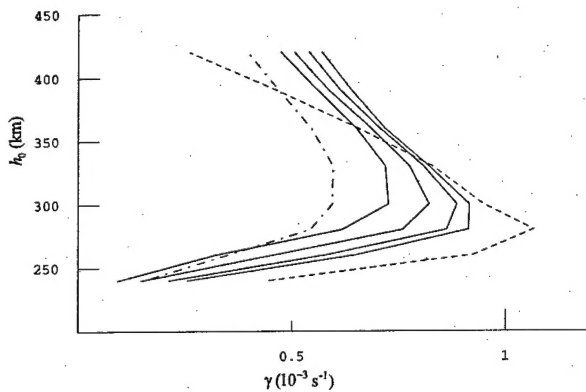


**Figure 2.** Altitude profiles of growth rates ( $\gamma$ ) for the ionospheric parameters shown in Figure 1. The dashed curve represents the local growth rate ( $\gamma_L$ ), the dot-dashed curve represents the flux tube integrated growth rate ( $\gamma_F$ ), and the solid curves represent the ballooning-mode type growth rate ( $\gamma_B$ ) for the perpendicular (east-west) wavelengths (300 m, 500 m, 1 km, and 2 km). The outermost solid curve is for 300 m, while the innermost one is for 2 km.

flux tube integrated growth rate provides a lower bound to the true value of the growth rate, while the local growth rate provides an upper bound. Our results give more detailed and more accurate comparisons. If we denote the altitudes at which the growth rates are maximum by  $h_{mL}$  (for local description),  $h_{mF}$  (for flux tube integrated description) and  $h_{mB}$  (for ballooning-mode type description), then we find that  $h_{mL} < h_{mB} < h_{mF}$ . Furthermore, the unstable regions predicted by both the flux tube integrated description and the ballooning-mode type description are higher in apex altitudes than that predicted by the local description. In particular, the local growth rate ( $\gamma_L$ ) becomes negative (meaning stability) above  $\sim 450$  km which is the altitude of the peak density of the F layer at equatorial latitude. However, both  $\gamma_B$  and  $\gamma_F$  remain positive well above 450 km. The two panels of Figure 3 show the spatial profiles of  $\phi_1$ , normalized to its maximum value  $\phi_{1m}$ , along the field lines whose apex altitudes ( $h_0$ ) are 300 and 420 km, respectively. The labeled curves in each panel are for  $\lambda_\psi = 300$  m, 500 m, 1 km, and 2 km. The panel for  $h_0 = 300$  km shows that the short wavelength modes are well localized near the magnetic equator ( $\hat{s} = 0$ ). Thus the equipotential assumption is not at all valid for the description of these modes. For longer wavelengths, the modes are more and more extended along the field line. The panel for  $h_0 = 420$  km shows that the maximum amplitude of the modes occurs at a distance away from the magnetic equator when the wavelengths are short. However, when the wavelengths are longer (than 2 km), the mode amplitudes tend to maximize near the equator as in the case of  $h_0 = 300$  km and the modes acquire flat-top profiles extending to larger distances along the field line. It may be argued that for these long wavelength modes the equipotential assumption is valid over the distances where  $\phi_1$  is roughly constant. The mode profiles can be understood by examining the structure of equation (45) and by considering the profiles of  $\nu_{in}$  and  $1/L_n$ .

[19] The four panels in Figure 4 show the ionospheric parameters ( $n_0$ ,  $1/L_n$ ,  $\nu_{in}$  and  $\nu_e$ ) as a function of  $\hat{s}$  ( $\equiv s/l$ ), where  $2l$  is the length of the field line, for the geophysical



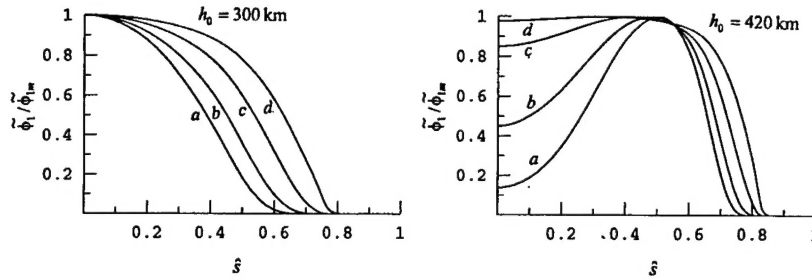


**Figure 3.** Profiles of the perturbed potential  $\tilde{\phi}_1$ , normalized to its maximum value  $\tilde{\phi}_{1m}$ , along the field lines whose apex altitudes ( $h_0$ ) are 300 and 420 km. The labeled curves in each panel are for the perpendicular (east-west) wavelengths: (a) 300 m, (b) 500 m, (c) 1 km, and (d) 2 km.

conditions of 20 April 2001. In this case the peak density of the  $F$  layer, at equatorial latitude, occurs at an altitude of  $\sim 500$  km. As before, the five curves in each panel are for five different field lines distinguished by their apex altitudes. The apex altitudes are higher in this case, since the vertical drift speed is larger ( $\sim 28$  m/s compared to  $\sim 11$  m/s in the previous case). The curves are qualitatively similar to those in Figure 1. These parameters are used in obtaining Figures 5 and 6. Figure 5 shows the three growth rates as a function of the apex altitude  $h_0$ . As in the previous case, the local description overestimates the growth rates up to a certain altitude and then underestimates them. The flux tube integrated description underestimates the growth rates at all altitudes, except at the very low and at the very high altitudes where the growth rates are small. The unstable region is higher in altitude and the maximum growth rates are larger compared to those in the previous case. These are explained by the fact that the vertical drift speed is larger in the second case. The larger vertical drift speed increases the growth rate by increasing its own contribution to the growth rate and also by increasing the gravitational part of the growth rate by raising the plasma layer to a higher altitude where  $v_{in}$  is smaller. Finally, the two panels of Figure 6 show the profiles of the unstable modes (for  $\lambda_\psi = 300$  m, 500 m, 1 km, and 2

km) along field lines whose apex altitudes are 420 and 500 km, respectively. These profiles are qualitatively similar to those in the previous case (Figure 3).

[20] We conclude this section with some additional results that may be of interest to the modelers. In the above calculations of the flux tube integrated growth rates, the upper limit of the field line integrations has been taken to be  $\zeta_{100}$  (value of  $\zeta$  at which the height of the field line is 100 km) because the model ionospheres virtually vanish below 100 km. If this upper limit is changed to  $\zeta_h$ , where  $h > 100$  km, the integrated Pedersen conductivity  $\Sigma_{PO}$ , which appears in the denominator of the gravitational part of the growth rate, decreases since the contribution from the  $E$  region is reduced. The corresponding decrements are relatively small in the case of  $L_N$  and  $I_{P0}^v$ . The net result is that  $\gamma_F$  increases. Physically, this may be described as due to the reduction in the damping effect of the  $E$  region. This suggests that if for certain modeling purposes we are willing to ignore the important physical effect of the  $E$  region,  $\gamma_F$  can be brought into a good agreement with  $\gamma_B$  by choosing a suitable value of  $\zeta_h$ . The spatial profiles of the perturbed potential  $\tilde{\phi}_1$  may provide a possible clue for this choice of  $\zeta_h$ . To be specific, since for the long wavelength ( $\lambda_\psi = 2$  km) modes  $\tilde{\phi}_1$  is almost constant for  $\tilde{s} \sim 0 - 0.7$  (see the panel labeled  $h_0 = 420$  km of Figure 3 and

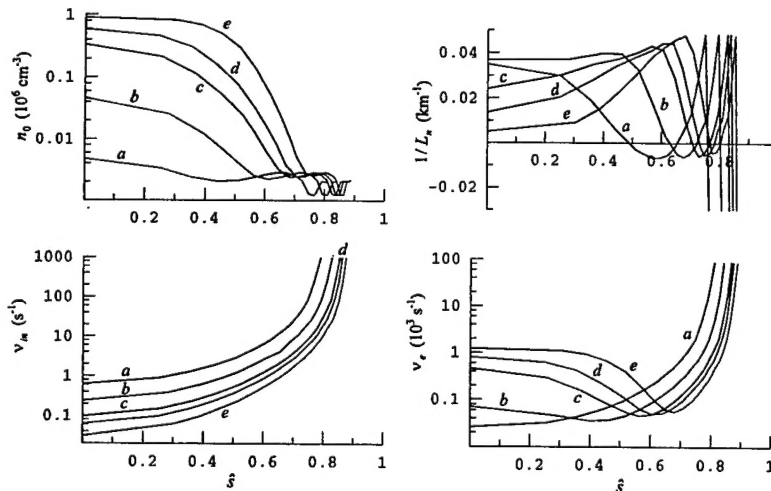


**Figure 4.** Profiles of the ionospheric parameters ( $n_0$ ,  $1/L_n$ ,  $v_{in}$  and  $v_e$ ) along a field line for the geophysical conditions on 20 April 2001 at 1900 LT. The labeled curves in each panel are for the field lines whose apex altitudes ( $h_0$ ) are (a) 300 km, (b) 360 km, (c) 420 km, (d) 450 km, and (e) 500 km.

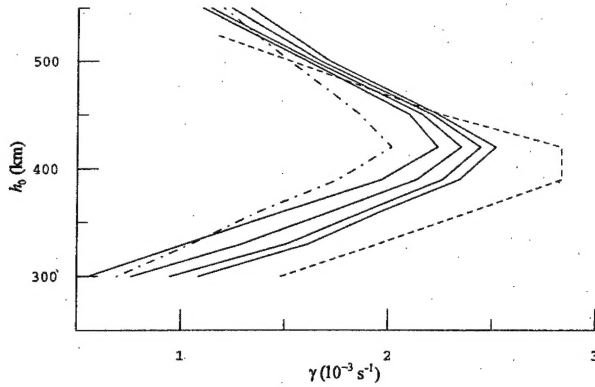


**Figure 5.** Same as in Figure 2, except that the growth rates ( $\gamma$ ) are obtained for the ionospheric parameters shown in Figure 4.

the panel labeled  $h_0 = 500$  km of Figure 6), it is reasonable to expect that  $\gamma_F$  would be in close agreement with  $\gamma_B$  if values of  $\zeta_h$  corresponding to  $\hat{s} \approx 0.7$  at those apex altitudes are chosen. Indeed, for those choices of  $\zeta_h$ ,  $\gamma_F$  is found to be within 5% of  $\gamma_B$  at those apex altitudes. However,  $\gamma_F$  cannot be expected to agree with  $\gamma_B$  at lower apex altitudes for the same  $\zeta_h$ , since the profiles of  $\phi_1$  are different. In other words, there does not exist a single value of  $\zeta_h$  for which  $\gamma_F$  would be in close agreement with  $\gamma_B$  at all apex altitudes. Different values of  $\zeta_h$  have to be chosen for different apex altitudes and they can be found only by trial and error. These are illustrated in Figure 7. In Figure 7a the solid curve represents  $\gamma_B$  (for  $\lambda_\psi = 2$  km) as a function of  $h_0$  for the geophysical parameters given in Figure 1. The dashed curve represents  $\gamma_F$  as a function of  $h_0$  if  $\zeta_{200}$ , which corresponds to  $\hat{s} \approx 0.7$  when  $h_0 = 420$  km, is used as the upper limit in the field line integrations. It shows good agreement with  $\gamma_B$  near 420 km, but poor agreement at lower altitudes. The dot-dashed curve in Figure 7a, on the other hand, shows excellent agreement with  $\gamma_B$  at all altitudes. This curve is obtained by using  $\zeta_{130}$  for  $h_0 \leq 330$  km and  $\zeta_{150}$  for  $h_0 > 330$  km as the upper limits in the field line integrations. In Figure 7b the solid curve represents  $\gamma_B$  as a function of  $h_0$  for the geophysical parameters used in Figure 4. The dashed curve represents  $\gamma_F$  as a function of  $h_0$  if  $\zeta_{240}$ , which corresponds to  $\hat{s} \approx 0.7$  when  $h_0 = 500$  km, is used as the upper limit in the field line integrations. Again, it shows good agreement with  $\gamma_B$  near 500 km, but poor agreement at lower altitudes. The dot-dashed curve in Figure 7b

showing excellent agreement with  $\gamma_B$  at all altitudes, on the other hand, is obtained by using  $\zeta_{140}$  for  $h_0 \leq 420$  km and  $\zeta_{170}$  for  $h_0 > 420$  km as the upper limits in the field line integrations. These findings are, of course, specific to the model ionospheres used in this paper.

## 5. Summary and Discussion

[21] In this paper we have presented for comparisons the three different theoretical descriptions of the linear stage of the equatorial plasma instability. Among the three, the local description, which is usually adopted in the study of interchange instability such as the Rayleigh-Taylor instability, is physically the most inadequate description of the instability in inhomogeneous plasma such as that found in the equatorial ionosphere. Nevertheless, it gives us important understanding of the basic mechanism of the instability. The flux tube integrated description, introduced by Haerendel (preprint, 1973) and often used in linear growth rate calculations, incorporates the effects of plasma inhomogeneity along the field line only in a gross manner. Besides, the flux tube integration is made possible by the equipotential assumption, which breaks down as the dipole magnetic field line curves into lower altitudes of increasing resistivity. In contrast, the ballooning-mode type description [Basu and Coppi, 1983, 1984; Basu, 1998] does not make the equipotential assumption; instead, allows for the variation of perturbed density and electrostatic potential along the magnetic field line and includes the full impact of the spatial inhomogeneity along the field line on the growth rates. So, on the basis of physical considerations, it may be argued that the ballooning-mode type description is comparatively the most accurate description of plasma instability in the equatorial ionosphere where the inhomogeneous plasma is embedded in a dipole magnetic field. The growth rates obtained from this description should, therefore, be the most accurate growth rates. Quantitative comparisons (Figures 2 and 5) show that the local description overestimates the growth rates up to a certain altitude and then underestimates them, while the flux tube integrated description underestimates the growth rates at almost all altitudes where the growth rates are significant. Moreover, unlike the local and the flux tube integrated descriptions, the ballooning-mode type description yields wavelength-dependent growth rates. So, for a given ionosphere the magnitude of the differences in the growth rates also depends on the perpendicular wavelengths of the unstable modes. For the model ionosphere given in Figure 1, the differences between  $\gamma_F$

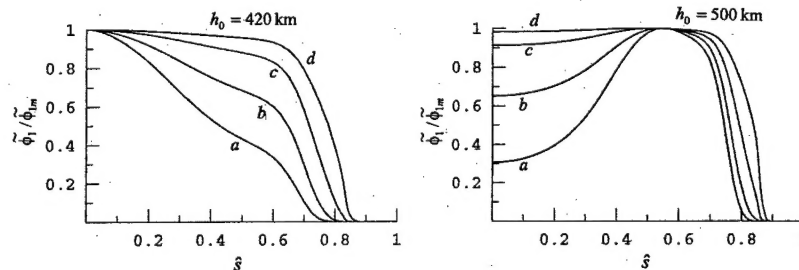


**Figure 6.** Profiles of the perturbed potential  $\tilde{\phi}_1$ , normalized to its maximum value  $\tilde{\phi}_{1m}$ , along the field lines whose apex altitudes are ( $h_0$ ) 420 and 500 km. The labeled curves in each panel are for the perpendicular (east-west) wavelengths: (a) 300 m, (b) 500 m, (c) 1 km, and (d) 2 km.

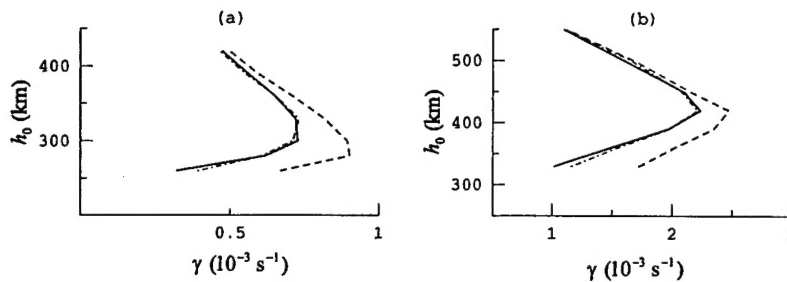


**Figure 7.** Dependence of flux tube integrated growth rate ( $\gamma_F$ ) on the upper limit of integration: (a) ionospheric parameters given in Figure 1 and (b) ionospheric parameters given in Figure 4. The solid curve is the altitude profile of  $\gamma_B$  for  $\lambda_\psi = 2$  km. In Figure 7a the dashed curve represents  $\gamma_F$  as a function of  $h_0$  when  $\zeta_{200}$  is used as the upper limit of integration and the dot-dashed curve represents the same when  $\zeta_{130}$  for  $h_0 \leq 330$  km and  $\zeta_{150}$  for  $h_0 > 330$  km are used as the upper limits of integrations. In Figure 7b the dashed curve represents  $\gamma_F$  as a function of  $h_0$  when  $\zeta_{240}$  is used as the upper limit of integration and dot-dashed curve represents the same when  $\zeta_{140}$  for  $h_0 \leq 420$  km and  $\zeta_{170}$  for  $h_0 > 420$  km are used as the upper limits of integrations.

(flux tube integrated growth rate) and  $\gamma_B$  (ballooning-mode type growth rate) are in the 24–40% range when the wavelength is 300 m and in the 12–18% range when the wavelength is 2 km. In terms of the growth period (one e-folding time), the differences are in the 7–12 min range when the wavelength is 300 m and in the 3–5 min range when the wavelength is 2 km. If 8–10 growth periods, say, are needed for the nonlinear saturation of the instability, the differences in the saturation time can be quite significant. For the other model ionosphere given in Figure 4 the differences are somewhat smaller but are still significant. Furthermore, only the ballooning-mode type description provides information on the spatial profiles of the excited modes. The localized spatial structures of the linear modes, that are found in the ballooning-mode type description and which are made possible by the sharp increase of plasma resistivity (namely,  $R(s)$  in equation (45)) along the curved magnetic field line, are expected to impose topological constraints on the nonlinear evolution of the instability and thus to play an important role in the determination of the nonlinear state of the plasma. In summary, the ballooning-mode type description provides a physically more accurate and more complete description of the equatorial plasma instability. Since the instability and its consequences are usually observed in the fully developed nonlinear stage, any observational evidence in support of the above conclusion has to come from the comparison of the predictions of the nonlinear study of the instability using the three theoretical formulations with the observations. Although the nonlinear evolution of the instability using the local and the flux tube integrated descriptions has been studied by several authors [see Keskinen *et al.*, 1998, and the references therein], similar study using the ballooning-mode type description is yet to be performed. The ballooning-mode type description of the nonlinearly saturated state of the instability may predict certain features, concerning either the spatial structures of the bubbles and plumes or the power spectrum of density and electric field fluctuations or both, that are distinct from those predicted by the other two descriptions. Ground-or space-based experiments may then be planned to observe these distinct features.

[22] **Acknowledgments.** The author gratefully acknowledges useful collaboration with B. Coppi and thanks N. Grossbard for his help with the numerical analysis. The author also thanks the referees for their useful and interesting suggestions. This work was supported in part by the Air Force Office of Scientific Research.

[23] Janet G. Luhmann thanks Robert E. Daniell Jr. and Joseph D. Huba for their assistance in evaluating this paper.

## References

- Basu, B., Generalized Rayleigh-Taylor instability in the presence of time-dependent equilibrium, *J. Geophys. Res.*, **102**, 17,305, 1997.
- Basu, B., Equatorial plasma instability in time-dependent equilibrium, *Phys. Plasmas*, **5**, 2022, 1998.
- Basu, B., and B. Coppi, Localized plasma depletion in the ionosphere and the equatorial spread F, *Geophys. Res. Lett.*, **10**, 900, 1983.
- Basu, B., and B. Coppi, Plasma depletion processes in the ionosphere and the equatorial spread F, *Rep. PTP-84/18*, MIT, Cambridge, Mass., 1984.
- Coppi, B., J. Filreis, and F. Pegoraro, Analytical representation and physics of ballooning modes, *Ann. Phys. N.Y.*, **121**, 1, 1979.
- Daniell, R. E., Jr., L. D. Brown, D. N. Anderson, M. W. Fox, P. H. Doherty, D. T. Decker, J. J. Sojka, and R. W. Schunk, Parameterized ionospheric model: A global ionospheric parameterization based on first principles models, *Radio Sci.*, **30**, 1499, 1995.
- Fejer, B. G., L. Scherliess, and E. R. de Paula, Effects of the vertical plasma drift velocity on the generation and evolution of equatorial spread F, *J. Geophys. Res.*, **104**, 19,859, 1999.
- Haerendel, G., J. V. Eccles, and S. Çakir, Theory for modeling of the equatorial evening ionosphere and the origin of the shear in the horizontal plasma flow, *J. Geophys. Res.*, **97**, 1209, 1992.
- Hedin, A. E., MSIS-86 thermospheric model, *J. Geophys. Res.*, **92**, 4649, 1987.
- Huba, J. D., P. A. Bernhardt, S. L. Ossakow, and S. T. Zalesak, The Rayleigh-Taylor instability is not damped by recombination in the F-region, *J. Geophys. Res.*, **101**, 24,553, 1996.
- Kelley, M. C., *The Earth's Ionosphere: Plasma Physics and Electrodynamics*, p. 127, Academic, San Diego, Calif., 1989.
- Keskinen, M. J., S. L. Ossakow, S. Basu, and P. J. Sultan, Magnetic-flux-tube-integrated evolution of equatorial ionospheric plasma bubbles, *J. Geophys. Res.*, **103**, 3957, 1998.
- Rappaport, H. L., Field line integration and localized modes in the equatorial spread F, *J. Geophys. Res.*, **101**, 24,545, 1996.
- Schunk, R. W., and A. F. Nagy, Ionospheres of terrestrial planets, *Rev. Geophys.*, **18**, 813, 1980.
- Sultan, P. J., Linear theory and modeling of the Rayleigh-Taylor instability leading to the occurrence of equatorial spread F, *J. Geophys. Res.*, **101**, 26,875, 1996.